


An investigation into the temperature phase transitions of synthesized lithium titanate materials doped with Al, Co, Ni and Mg by *in situ* powder X-ray diffraction

X. van Niekerk ^{1,a)} E. E. Ferg,¹ C. Gelant,¹ and D. G. Billing²

¹Department of Chemistry and uYilo, e-Mobility Technology Innovation Programme, Nelson Mandela University, P.O. Box 77000, Port Elizabeth 6001, South Africa

²School of Chemistry and DST/NRF Centre of Excellence in Strong Materials, University of Witwatersrand, Private Bag 3, Johannesburg 2000, South Africa

(Received 31 July 2019; accepted 6 July 2020)

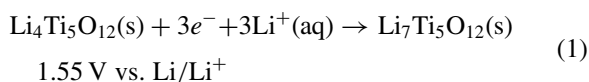
Li₄Ti₅O₁₂ (LTO) and its doped analogues Li₄Ti_{4.95}M_{0.05}O₁₂ (M = Al³⁺, Co³⁺, Ni²⁺, and Mg²⁺) were synthesized and characterized using *in situ* PXRD to monitor the phase transitions during the sol–gel synthesis of the spinel material. These results are complimented by thermogravimetric analysis, which illustrates the decomposition of the materials synthesized, where the final LTO products are seen to form at approximately 550 °C. The material has an amorphous structure from room temperature, coupled with a crystalline phase which is speculated to be H₂Ti₂O₅ · H₂O. This crystalline phase disappears at 250 °C, with the material still in the amorphous state. The crystalline LTO phase starts at approximately 550 °C, with anatase co-crystallizing with the spinel phase. Rutile appears at 600 °C and co-crystallizes with the final product at 850 °C, where anatase is no longer seen. The rutile impurity remains present after cooling the material to room temperature, and results indicate that prolonged heating at 850 °C is required to reduce the rutile content. Rietveld refinement of diffraction patterns show that the unit-cell parameter increases with increasing temperature, coupled with a decrease when cooling the sample. The crystallite sizes follow the same trend, with a significant increase above temperatures of 750 °C. © 2020 International Centre for Diffraction Data.

[doi:10.1017/S0885715620000494]

Key words: *in-situ* powder X-ray diffraction, Al, Co, Ni and Mg-doped Li₄Ti₅O₁₂, unit-cell parameter, amorphous and crystalline precursors, rutile and anatase

I. INTRODUCTION

Spinel Li₄Ti₅O₁₂ (LTO) is a promising anode material for lithium-ion batteries due to its zero-strain electrochemical capability, inherent safety, and excellent cyclic performance (Nugroho *et al.*, 2014, Wang *et al.*, 2015). The material has a face-centred structure with an *Fd3m* (227) cubic space group. The lithium ions are located at the tetrahedral 8a sites (Figure 1), the lithium and tetravalent titanium ions are randomly dispersed at the 16d octahedral sites and the oxygen ions are located at the 32e sites, with a unit-cell parameter of 8.358 Å (Yi *et al.*, 2010). Upon lithium insertion during discharge, the lithium ions move from the 8a to the 16c sites forming Li₇Ti₅O₁₂, a rock salt structure, where all 16c sites are occupied and all 8a sites are empty (Ganapathy and Wagemaker, 2012), as shown in the following reaction:



In an electrochemical cell, the spinel LTO gives a flat charge–discharge curve at 1.55 V vs. Li/Li⁺ owing to the

stability of the Ti⁴⁺/Ti³⁺ couple during capacity cycling (Sun *et al.*, 2015); however, the high oxidation state (+4) of the titanium in the spinel structure acts as an insulator that effectively results in poor electronic conductivity ($\approx 10^{-13}$ S cm⁻¹), which is one of the main problems encountered with this material as it restricts electron transfer for high rate applications (Yi *et al.*, 2010; Sun *et al.*, 2015). Various methods have been proposed to improve the conductivity, including carbon surface modification, compositing, and doping the material with metals, non-metals, and metal oxides (Ming *et al.*, 2014; Sun *et al.*, 2015; Xie *et al.*, 2015; Ni *et al.*, 2016; Coelho *et al.*, 2017).

The understanding of the synthetic route to form the spinel Li₄Ti₅O₁₂ and its doped congeners is an important aspect to consider due to the influence it would have on the final electrochemical properties of the active material. The most commonly used synthetic methods include a range of solid-state reactions, hydro- or solvo-thermal methods, sol–gel synthesis, and spray pyrolysis (Hao *et al.*, 2005; Rai *et al.*, 2012; Han *et al.*, 2013; Mosa *et al.*, 2013; Zhang *et al.*, 2013; Li *et al.*, 2014; Priyono *et al.*, 2015; Kuo *et al.*, 2016). Solid-state reaction methods have predominated due to the ease of mixing the solid material in a given ratio; however, it has limitations in terms of the resultant materials particle size and shape, its uniformity and the required prolonged calcination times (Hao *et al.*, 2005; Yi *et al.*, 2010). Sol–gel synthesis overcomes

^{a)}Author to whom correspondence should be addressed. Electronic mail: xandri.vanniekerk@mandela.ac.za

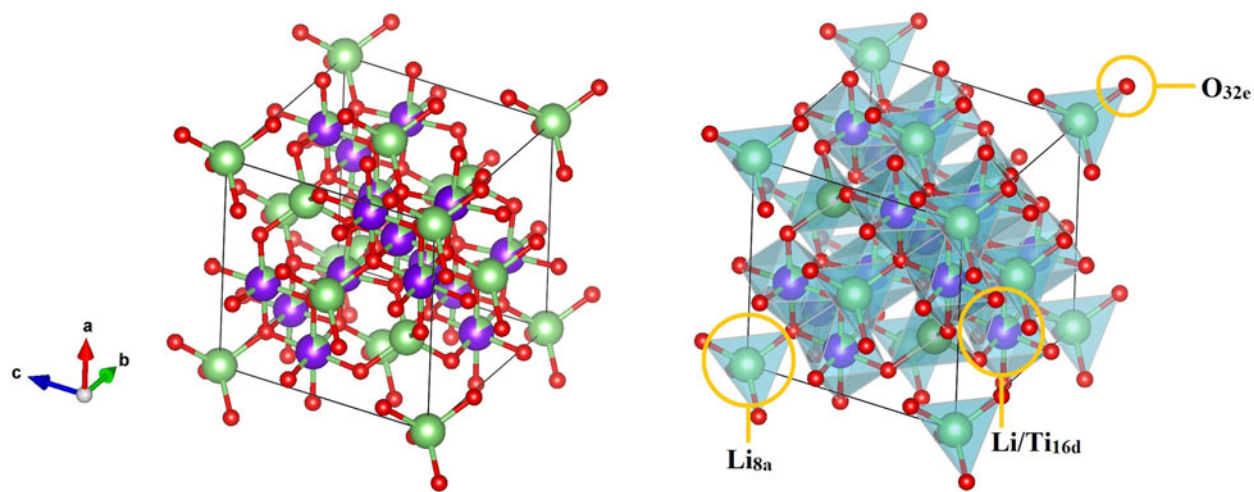


Figure 1. Structure of spinel $\text{Li}_4\text{Ti}_5\text{O}_{12}$ showing atoms in the unit cell only (left) and unit cell with the polyhedra (right) where the tetrahedra indicates the 8a sites occupied by Li^+ and the octahedra indicates the 16d sites that are occupied by Li^+ and Ti^{4+} . The O^{2-} anions occupy the octahedral 32e sites (Deschavres *et al.*, 1971; Koichi Momma, 2011).

many of these limitations by producing a material that is homogeneous with cubic-shaped particles, although it can be more expensive when required to make the material on a large scale (Sun *et al.*, 2015). Chelating agents such as acetic acid and triethanolamine (TEA) have been used in the sol-gel synthesis of lithium titanium oxide, where their main functions are to coordinate to Ti^{4+} ions, thereby preventing hydrolysis to $\text{Ti}(\text{OH})_4$ (Shen *et al.*, 2003; Hao *et al.*, 2005). This method requires high calcining temperatures around 800 °C for long times to form the final lithium titanium oxide powder, with good homogeneity and uniform, sub-micron-sized particles (Shen *et al.*, 2003; Hao *et al.*, 2005; Mahmoud *et al.*, 2015). This makes the development of batteries with this type of material for large-scale applications difficult where

its manufacturing cost would be very high when compared to the conventional use of carbon as anodes. An in-depth knowledge of the phase transitions involved in the sol-gel synthesis would be beneficial to optimize the manufacturing process. In order to identify and understand the temperature phase transitions that the material undergoes during the calcination synthesis process, *in situ* powder X-ray diffraction (PXRD) was shown to be a well-suited technique to study the phase transitions of lithium manganese oxide spinel used as cathode materials in lithium-ion batteries and was employed in this study (Snyders *et al.*, 2016).

This paper focuses on studying the doping effect of Ti^{4+} ions in LTO with 1% Al^{3+} , Mg^{2+} , Co^{3+} , and Ni^{2+} ions using the sol-gel method as described by Hao *et al.* (2005). This

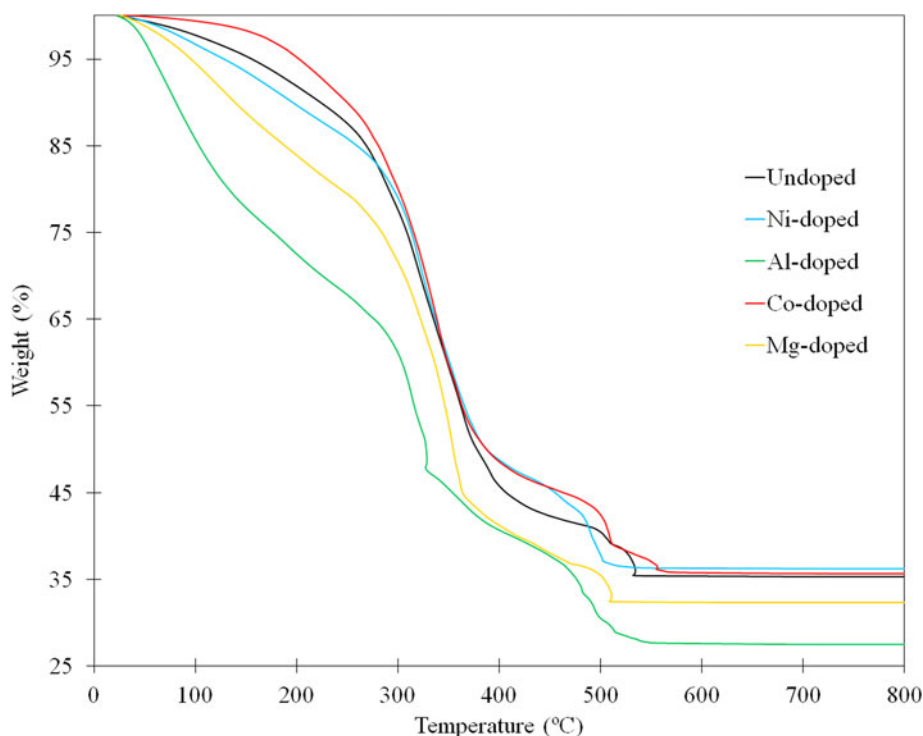


Figure 2. TGA curves of $\text{Li}_4\text{Ti}_5\text{O}_{12}$ and $\text{Li}_4\text{Ti}_{4.95}\text{M}_{0.05}\text{O}_{12}$ ($\text{M} = \text{Al}^{3+}$, Mg^{2+} , Ni^{2+} , and Co^{3+}).

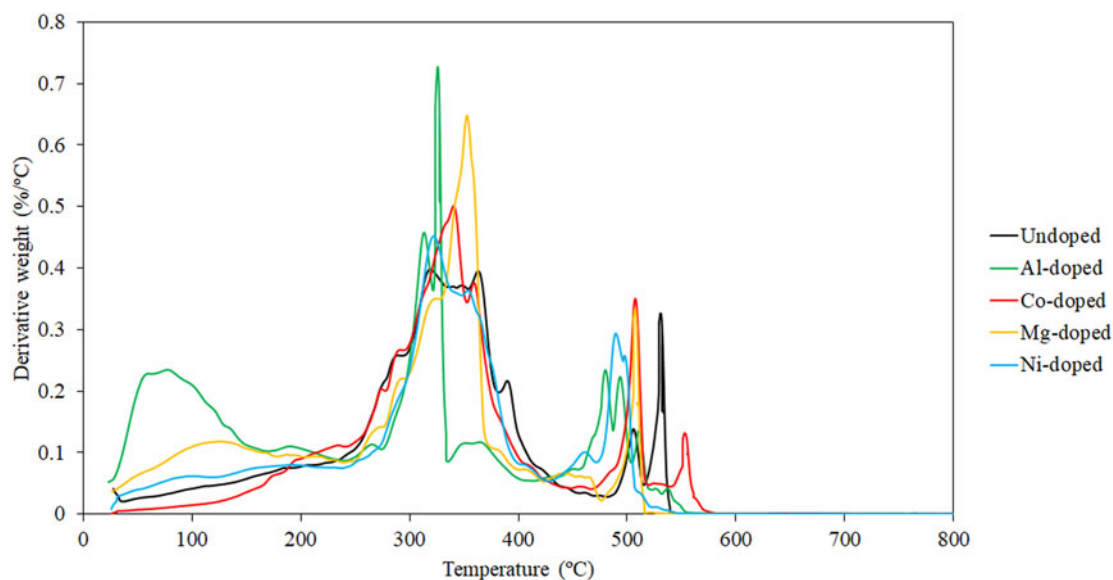


Figure 3. TGA derivative weight loss of undoped and doped spinel material.

study investigates the phase transitions that take place in the synthetic route of both the undoped material ($\text{Li}_4\text{Ti}_5\text{O}_{12}$) and the doped congeners. The percentage phase composition, unit-cell parameters, crystallite sizes (LVol-IB), and strain for the doped and undoped spinel LTO were refined and compared for the patterns obtained for the *in situ* study from 50 to 850 °C, followed by cooling to 50 °C.

II. EXPERIMENTAL

The undoped ($\text{Li}_4\text{Ti}_5\text{O}_{12}$) and doped spinel $\text{Li}_4\text{Ti}_{4.95}\text{M}_{0.05}\text{O}_{12}$ ($\text{M} = \text{Ni}, \text{Co}, \text{Mg}, \text{and Al}$) materials were prepared by a sol-gel method using triethanolamine as a complexing agent, similar to the methods described by Hao *et al.* (2005) and Lin *et al.* (2013). Titanium butoxide was dissolved in triethanolamine in a 4:5 ratio in an ethanolic solution to form solution A. For the doped materials, aluminium acetate, magnesium acetate tetrahydrate, nickel acetate tetrahydrate, and cobalt acetate tetrahydrate were weighed out in order to achieve a concentration of 1% (moles in relation to the titanium ion) Al^{3+} , Mg^{2+} , Ni^{2+} , and Co^{3+} , respectively. The acetates were added to these solutions to form the respective materials $\text{Li}_4\text{Ti}_{4.95}\text{Al}_{0.05}\text{O}_{12}$, $\text{Li}_4\text{Ti}_{4.95}\text{Mg}_{0.05}\text{O}_{12}$, $\text{Li}_4\text{Ti}_{4.95}\text{Ni}_{0.05}\text{O}_{12}$, and $\text{Li}_4\text{Ti}_{4.95}\text{Co}_{0.05}\text{O}_{12}$ (Hao *et al.*, 2005; Lin *et al.*, 2013). Dopants chosen were based on those reported in the literature

with improved material characteristics, which would lead to better electrochemical performance when used in a battery (Wang *et al.*, 2013; Abureden *et al.*, 2016; Liang *et al.*, 2017; Ncube *et al.*, 2018).

Lithium acetate dihydrate was dissolved in a 50:50 ethanol/water solution (solution B) and gradually dropped into the titanium solution until a clear mixture formed. The resulting mixture (solution C) was left to hydrolyze overnight until a gel-based precursor at room temperature formed. The precursor gels were placed in a drying oven at 85 °C for 6 h. Preparation of material for *in situ* analysis was done by further drying the precursor materials at 2 °C min^{-1} in a tube furnace until 300 °C was reached. PXRD analysis was done on the cooled room temperature material where its phase composition was determined to still be amorphous. The material was subsequently ground into a fine powder for easier sample mounting in the instrument. The *in situ* PXRD analysis was done on a Bruker D8 Advance with a Vantec detector, Cu radiation, and Goebel primary beam mirror. An Anton Parr XRK900 cell was used with a macor ceramic sample holder including a platinum (Pt) foil inset. *In situ* PXRD analysis entailed the heating of the precursor material in air (previously heated to 300 °C) in a chamber where the temperature was gradually increased by 10 °C min^{-1} from 30 to 850 °C. Upon heating, each diffraction pattern was collected at a

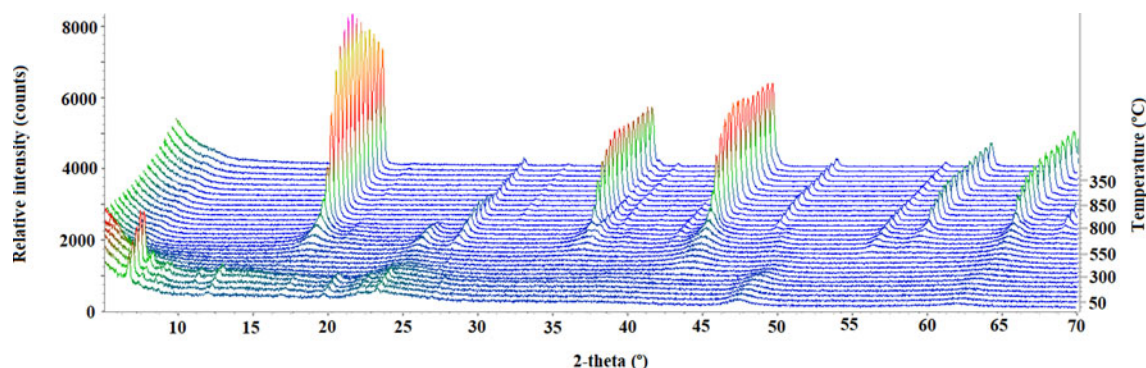


Figure 4. *In situ* PXRD VT-scan of $\text{Li}_4\text{Ti}_5\text{O}_{12}$ synthesized from the sol-gel precursor.

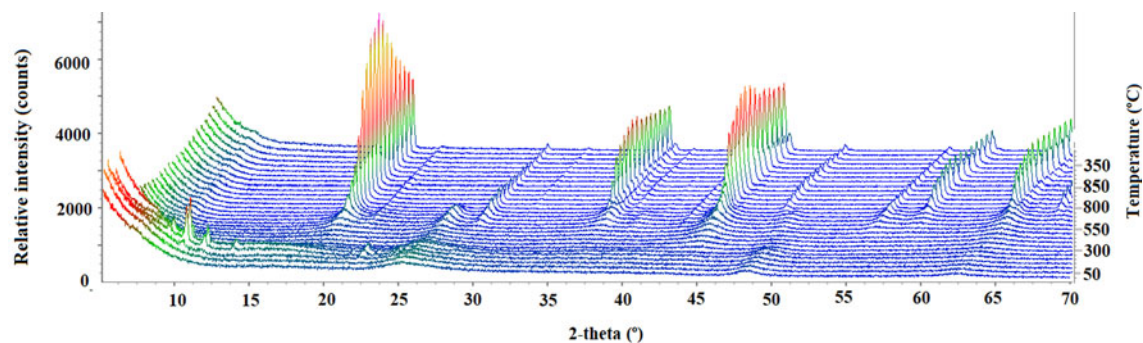


Figure 5. *In situ* PXRD VT-scan of $\text{Li}_4\text{Ti}_{4.95}\text{Al}_{0.05}\text{O}_{12}$ synthesized from the sol-gel precursor.

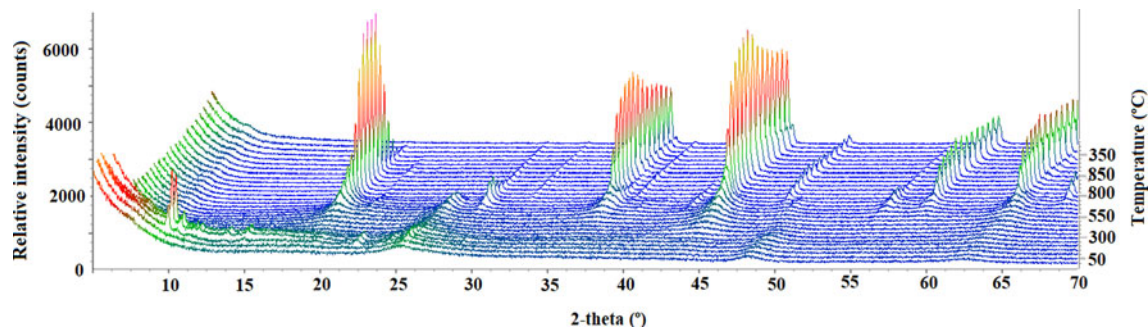


Figure 6. *In situ* PXRD VT-scan of $\text{Li}_4\text{Ti}_{4.95}\text{Co}_{0.05}\text{O}_{12}$ synthesized from the sol-gel precursor.

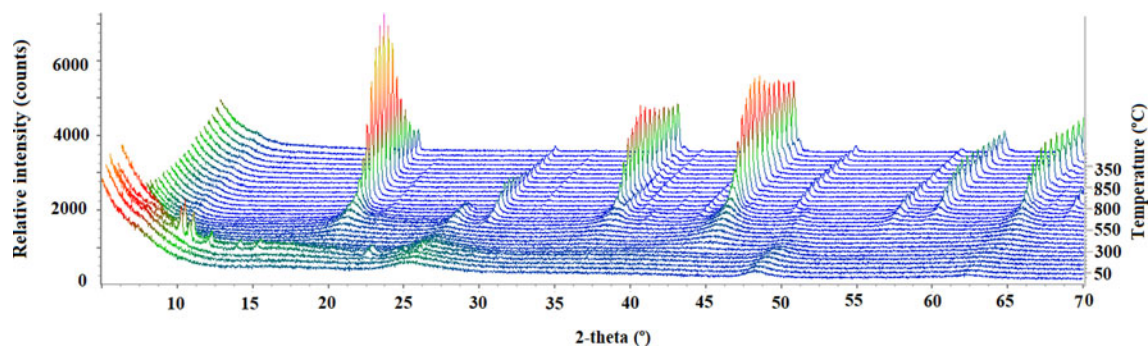


Figure 7. *In situ* PXRD VT-scan of $\text{Li}_4\text{Ti}_{4.95}\text{Mg}_{0.05}\text{O}_{12}$ synthesized from the sol-gel precursor.

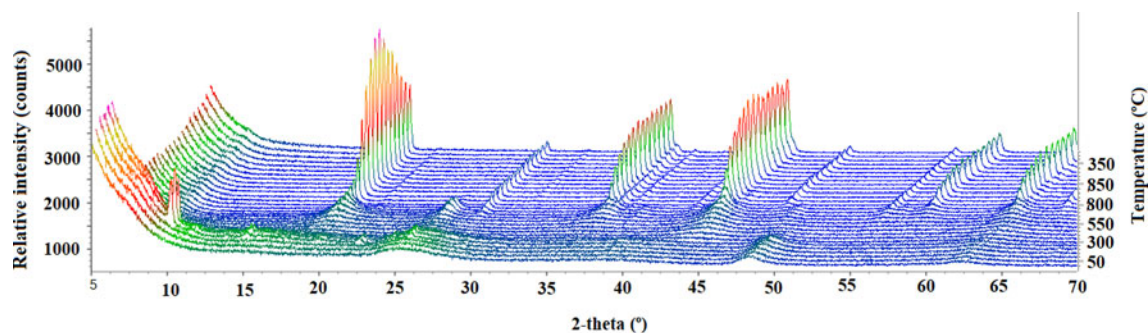


Figure 8. *In situ* PXRD VT-scan of $\text{Li}_4\text{Ti}_{4.95}\text{Ni}_{0.05}\text{O}_{12}$ synthesized from the sol-gel precursor.

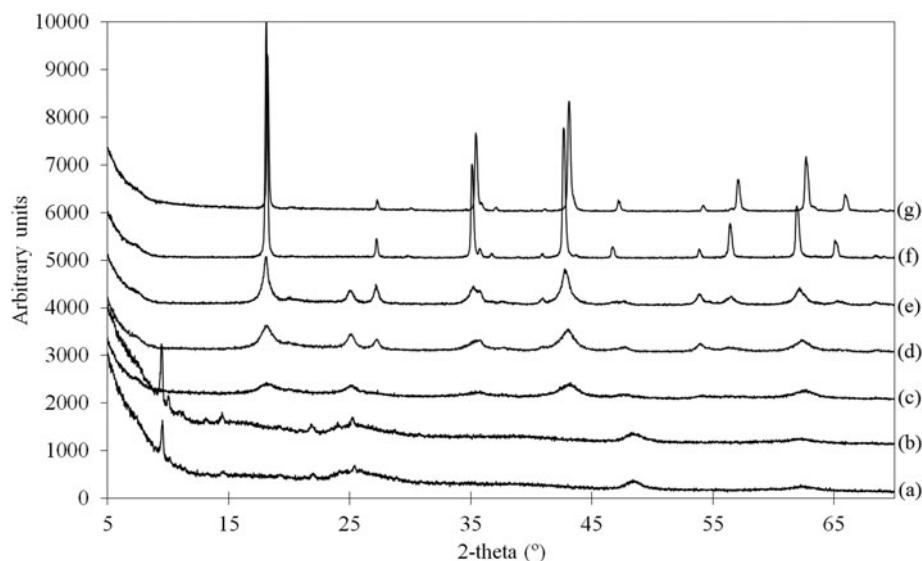


Figure 9. Selected PXRD patterns of the $\text{Li}_4\text{Ti}_5\text{O}_{12}$ gel precursor in staggered plot from the *in situ* results for (a) 30 °C, (b) 200 °C, (c) 550 °C, (d) 650 °C, (e) 750 °C, (f) 850 °C, and (g) 50 °C.

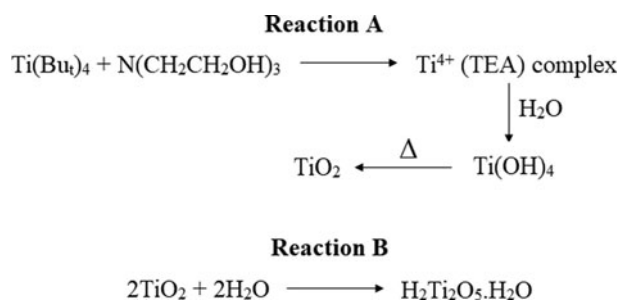


Figure 10. Reaction of titanium(IV) butoxide and triethanolamine to form titanium dioxide (Reaction A), which further reacts with water to form $\text{H}_2\text{Ti}_2\text{O}_5 \cdot \text{H}_2\text{O}$ (Reaction B).

fixed temperature every 50 °C intervals. The heating stage was kept isothermally for the duration of the analysis which lasted 10 min. The diffraction scan range was from 5–70° at 0.02° step^{-1} . At 850 °C, the heating stage was kept isothermally for 4 h with a diffraction pattern collected every hour. Subsequently, the heating stage was cooled at 10 °C min^{-1} to room temperature with a diffraction pattern collected at 100 °C intervals. *In situ* phase identifications and quantification were done by full pattern Rietveld refinement using Topas v.6 software (Bruker, 2016). This was done by allowing the respective lattice parameters, crystallite sizes (LVol-IB), and strain to refine. Refinement of the unit-cell parameters

and microstructural data were performed on patterns which were noticeable above the amorphous halo. The doped metal ions replaced the lithium sites at the 16d positions in the quantification of the doped material. The crystallographic open database (Downs and Hall-Wallace, 2003; Gražulis *et al.*, 2009; Gražulis *et al.*, 2012; Gražulis *et al.*, 2015; Merkys *et al.*, 2016) was used for the respective refinements and included the open database files 1001098 ($\text{Li}_4\text{Ti}_5\text{O}_{12}$) (Deschanvres *et al.*, 1971), 9004142 (rutile) (Meagher and Lager, 1979), 9009086 (anatase) (Wyckoff, 1963), and 1515995 (Li_2TiO_3) (Dorrian and Newnham, 1969).

Thermogravimetric analysis (TGA) of the precursor materials was done at 10 °C min^{-1} from room temperature to 800 °C in air using a TA instruments SDT Q600 and analysed using TA Universal Analysis v.4.5 software.

The Micrometrics Tristar II Brunauer–Emmett–Teller (BET) analyser was done to determine the surface area of the synthesized materials heated to 650 and 850 °C, respectively. Samples were degassed with nitrogen overnight at 350 °C.

III. RESULTS AND DISCUSSION

The weight loss with temperature TGA curves for the prepared materials show similarities between the undoped material and the magnesium-, nickel-, and cobalt-doped samples

TABLE I. Summary of BET results and Rietveld refined parameters from *in situ* X-ray diffraction results.

Sample	$\text{Li}_4\text{Ti}_5\text{O}_{12}$	$\text{Li}_4\text{Ti}_{4.95}\text{Al}_{0.05}\text{O}_{12}$	$\text{Li}_4\text{Ti}_{4.95}\text{Ni}_{0.05}\text{O}_{12}$	$\text{Li}_4\text{Ti}_{4.9}\text{Mg}_{0.05}\text{O}_{12}$	$\text{Li}_4\text{Ti}_{4.95}\text{Co}_{0.05}\text{O}_{12}$
Crystallite size (nm)					
at 650 °C	4.37	5.86	3.89	4.55	5.75
at 850 °C	58.4	149.91	62.55	78.44	114.51
Percentage LTO (%)					
at 650 °C	69.90	64.72	74.69	79.18	73.32
at 850 °C	93.95	82.14	90.92	92.52	97.30
BET surface area ($\text{m}^2 \text{g}^{-1}$)					
at 650 °C	12.79	55.15	1.17	1.29	5.61
at 850 °C	0.44	3.63	0.40	0.33	0.52

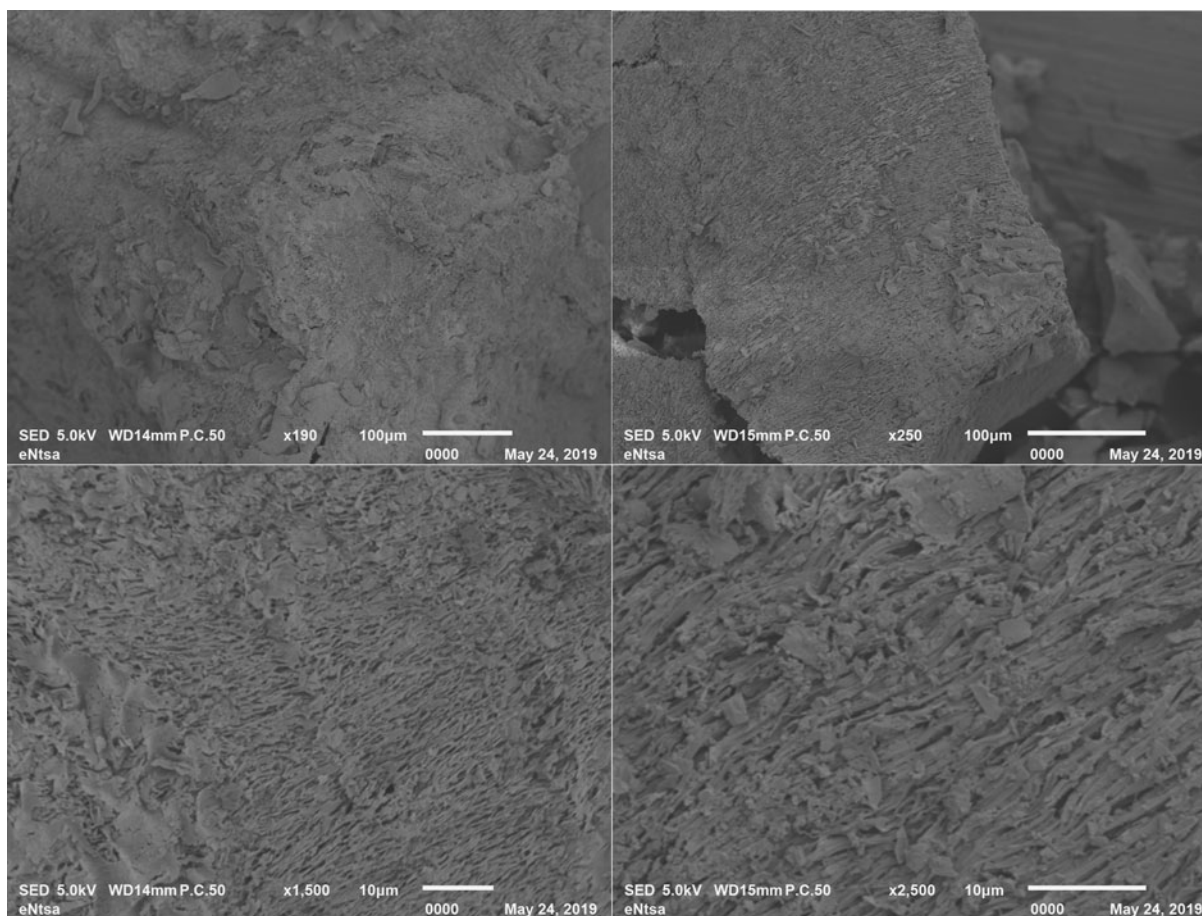


Figure 11. SEM images of the undoped LTO synthesized at 650 °C at (a) $\times 190$, (b) $\times 250$, (c) $\times 1500$, and (d) $\times 2500$ magnification.

(Figure 2). They all show the main decomposition step between room temperature and ± 400 °C of about 45–30%, which can be attributed to some of the water lost from the sol–gel precursor, as well as the loss of organic components. The second weight loss is seen above 400 °C for these materials, which is speculated to be further loss of organic-based materials as well as the oxidation of the final precursor compounds. $\text{Li}_4\text{Ti}_{4.95}\text{Al}_{0.05}\text{O}_{12}$ showed anomalous behaviour when compared to the other samples, as multiple weight loss steps were detected and at markedly lower temperatures. This can be seen by plotting the derivative weight loss with temperature, where the first mass loss observed was at approximately 100 °C for the Al-doped material (Figure 3) and can be ascribed to water loss. All five synthesized precursors show that around 550–600 °C no further weight loss from the samples were observed, which agrees with results obtained from the *in situ* studies, as the final material has been formed at this point, with slight variation in the temperature at which the spinel material is formed.

The *in situ* PXRD three-dimensional graph shows the phase transformation for the undoped material after initial drying at 300 °C (Figure 4). The results show the gradual formation of the spinel as well as the anatase phase from a predominant amorphous phase when heated from 30 to 850 °C. The sample was kept isothermal at 850 °C for 4 h followed by the gradual cooling to a temperature of 50 °C. The metal-doped analogues showed similar *in situ* results, as can be seen from Figures 5–8.

Selected diffraction patterns of the undoped LTO material are illustrated in Figure 9, which show the transition from the amorphous state through to the final spinel phase. The results show the amorphous material from 30 to 550 °C, with a series of peaks at low 2θ values that appeared in the patterns obtained at 30 [Figure 9(a)] and 200 °C [Figure 9(b)], respectively. These peaks around $9^\circ 2\theta$ disappeared once the sample was heated above 250 °C [Figure 9(c)]. Due to the low intensity of the peaks associated with this particular phase and the presence of the bulk amorphous material, the phase could not be accurately identified and quantified; however, it is speculated to be a type of titanium acid ($\text{H}_2\text{Ti}_2\text{O}_5 \cdot \text{H}_2\text{O}$) which was described in the literature to be a precursor material of typical titanate-based oxides (Song *et al.*, 2005; Etacheri *et al.*, 2013). The pattern obtained at 200 °C [Figure 9(b)] matched reasonably well with the diffraction pattern of $\text{H}_2\text{Ti}_2\text{O}_5 \cdot \text{H}_2\text{O}$ [PDF 00-047-0124 (ICDD, 2002)] (Song *et al.*, 2005; Etacheri *et al.*, 2013).

Titanium(IV) butoxide reacts with triethanolamine to form a stable titanium(IV) intermediate (Figure 10), which in turn reacts with water to form $\text{Ti}(\text{OH})_4$ (Sugimoto *et al.*, 2003). According to the literature, this intermediate further forms TiO_2 when heated (Sugimoto *et al.*, 2003). It was suggested that the anatase then reacts with water to give $\text{H}_2\text{Ti}_2\text{O}_5 \cdot \text{H}_2\text{O}$ (Figure 10). There are reported cases of TiO_2 co-existing with $\text{H}_2\text{Ti}_2\text{O}_5 \cdot \text{H}_2\text{O}$; however, the mechanism of its formation has not been well described in the literature (Haro-González *et al.*, 2011; Arruda *et al.*, 2015). Upon

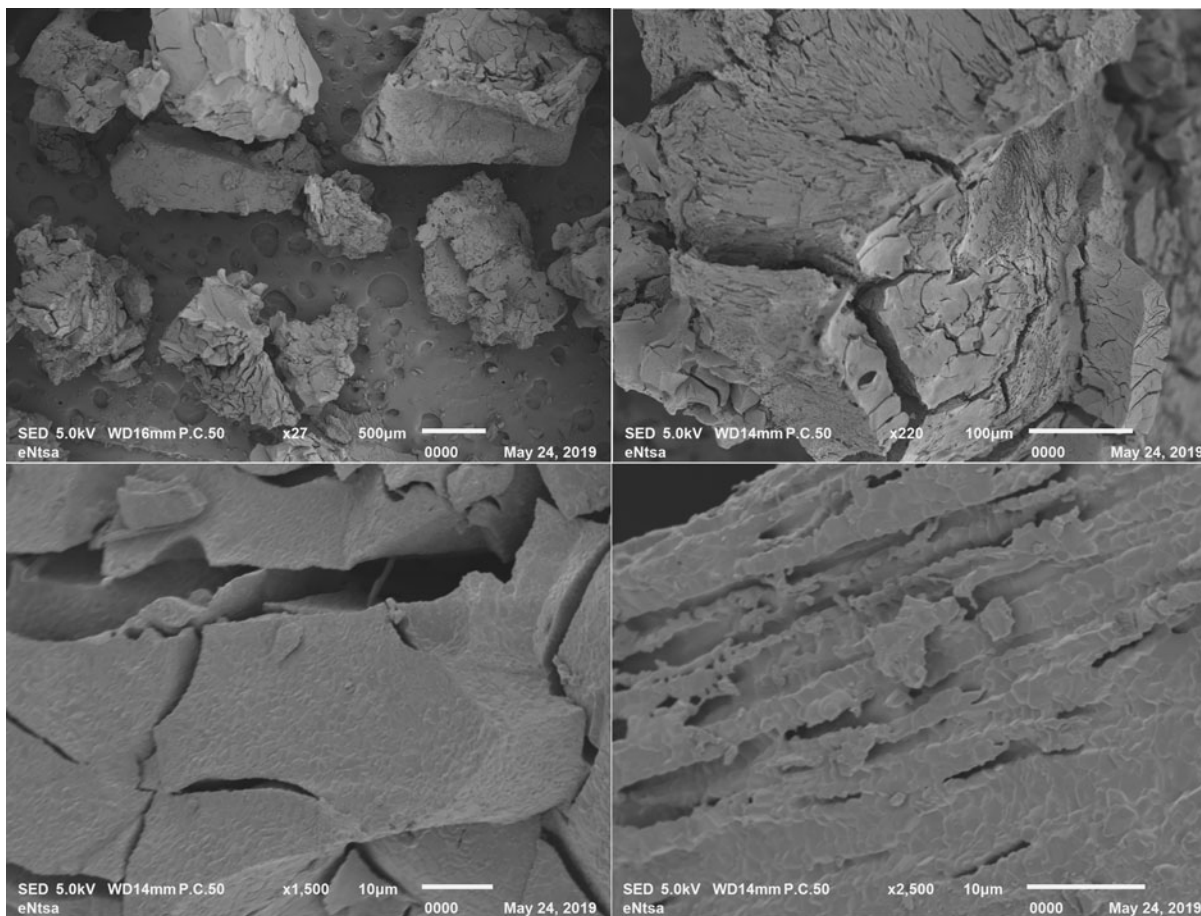


Figure 12. SEM images of the undoped LTO synthesized at 850 °C at (a) $\times 27$, (b) $\times 220$, (c) $\times 1500$, and (d) $\times 2500$ magnification.

further heating, this phase subsequently disappears at temperatures above 250 °C, where the titanate phase of anatase and the spinel are seen to form [Figures 6(c) and 6(d)].

At 550 °C, the diffraction peaks for the two phases anatase (30.34%) and spinel $\text{Li}_4\text{Ti}_5\text{O}_{12}$ (69.66%) could be reasonably quantified by full pattern Rietveld refinement. Upon further heating, the rutile phase appears (600 °C), with spinel LTO as the major phase (70.73%). The LTO crystalline phase is seen to form from 550 to 750 °C with relatively broad peaks [Figures 9(c) and 9(d)], where the sharper, more distinctive peaks can be seen from 850 °C [Figure 9(e)] onwards. There is a decrease in intensity observed upon cooling to room temperature for the main $\text{Li}_4\text{Ti}_5\text{O}_{12}$ peak at around $18^\circ 2\theta$ [Figure 9(f)]; however, the relative amounts of the material remains unchanged throughout the cooling process. Since

the crystallite size remains unchanged for the undoped material, the peak intensity decrease can possibly be attributed to sample displacement in the sample holder, due to shrinkage, combined with other cooling effects.

The LTO phase at 650 °C is the characteristic of material with relatively small crystallites based on the broad diffraction peaks observed. This correlates with BET surface area results, which show that material synthesized at 650 °C had, on average, a larger surface area ($12.79 \text{ m}^2 \text{ g}^{-1}$) when compared to its 850 °C analogue ($0.44 \text{ m}^2 \text{ g}^{-1}$) (Table I). Hence, the material with smaller crystallites would, on average, have a larger surface area. This can also be seen in the scanning electron microscopy (SEM) images that showed the material synthesized at 650 °C (Figure 11) to be significantly more porous than the material made at 850 °C (Figure 12) that showed a

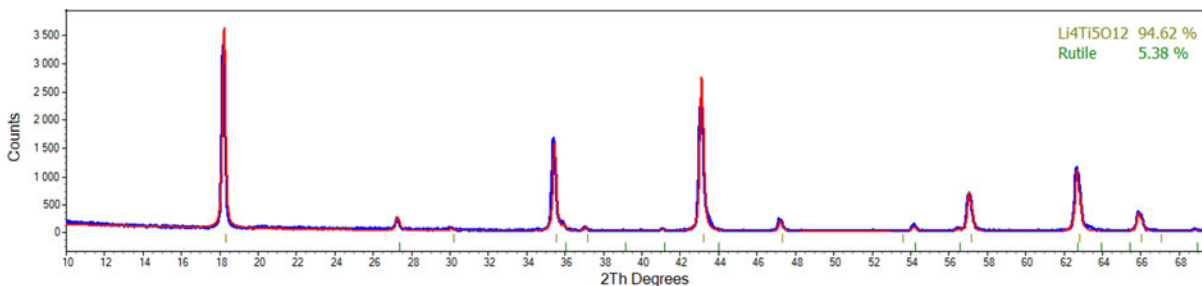


Figure 13. Rietveld refinement plot showing the phase composition of $\text{Li}_4\text{Ti}_5\text{O}_{12}$ after being cooled to 50 °C. The blue line shows the experimental data and the red line shows the fitted data.

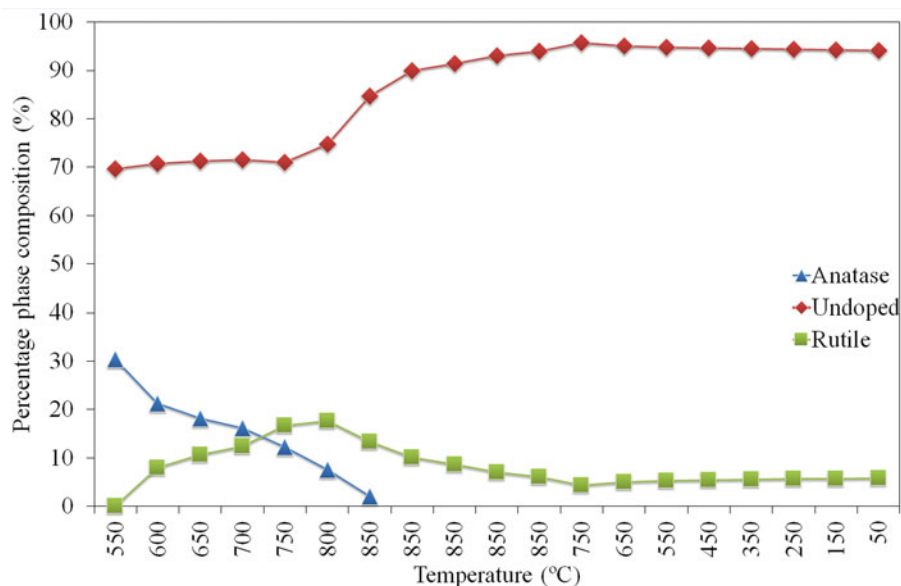


Figure 14. Percentage phase composition of the spinel LTO material, rutile, and anatase from 550 to 850 °C, followed by cooling to room temperature.

conglomeration of sintered particles. Energy-dispersive spectroscopy (EDS) analysis was done to show the uniform distribution of the dopant elements. The respective scans and their elemental mapping are shown in the Supplementary Material.

The anatase phase disappeared at around 750 °C, with only the spinel LTO and the appearance of the rutile phase. The phase transition of the anatase to rutile phase transition is reported in the literature to be around 750 °C (Khatun *et al.*, 2017). Upon further heating, the rutile phase would slowly convert to the spinel phase where the final product, once cooled to 50 °C, would show a typical phase composition of 94.62% LTO and 5.38% rutile, respectively (Figure 13). The three main peaks of $\text{Li}_4\text{Ti}_5\text{O}_{12}$ at around 17.5°, 35°, and 42.5° (Figure 13) can be assigned to crystallographic peaks (111), (311), and (400), respectively. There is a slight peak shift observed compared to the literature reported LTO due to sample cooling effects, which results in sample shrinkage and therefore sample displacement (Zhu *et al.*, 2019). The three distinct peaks at approximately 27° (110), 36° (101), and 54.5° (211) are ascribed to rutile still present in the material.

The quantitative phase transitions of the undoped LTO material with temperature can be summarized in Figure 14, showing a steady increase in the spinel phase from its formation at 550 up to 850 °C. Notably, the anatase phase would decrease above 550 °C with the appearance and increase of the rutile phase from 600 to 800 °C. The rutile phase in the sample would subsequently decrease when heated to 850 °C. By keeping the sample isothermally at 850 °C for 4 h, the rutile phase composition decreased by 45% from its initial value at 850 °C (13.32%). With the decreasing rutile content, an increase in the LTO phase is observed at the isothermal stage. This increase is still seen during the cooling process until 750 °C, after which a slight decrease is seen. This indicates that temperatures above 750 °C are sufficient to decrease the rutile content and increase the LTO phase, although 850°C would be more efficient.

Figure 15 illustrates the selected patterns from 30 up to 850 °C of the *in situ* results for $\text{Li}_4\text{Ti}_{4.95}\text{Ni}_{0.05}\text{O}_{12}$, where the material was heated to 300 °C prior to *in situ* studies to effectively dry the sample. The doped LTO material showed the amorphous material [Figure 15(a)] up to about 450 °C,

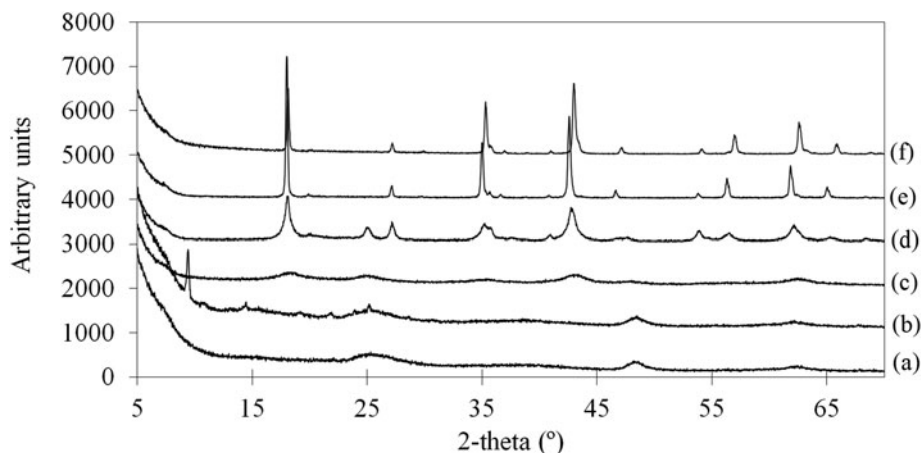


Figure 15. Selected PXRD patterns of the $\text{Li}_4\text{Ti}_{4.95}\text{Ni}_{0.05}\text{O}_{12}$ gel precursor in staggered plot from the *in situ* results for (a) 30 °C, (b) 200 °C, (c) 500 °C, (d) 750 °C, (e) 850 °C, and (f) 50 °C.

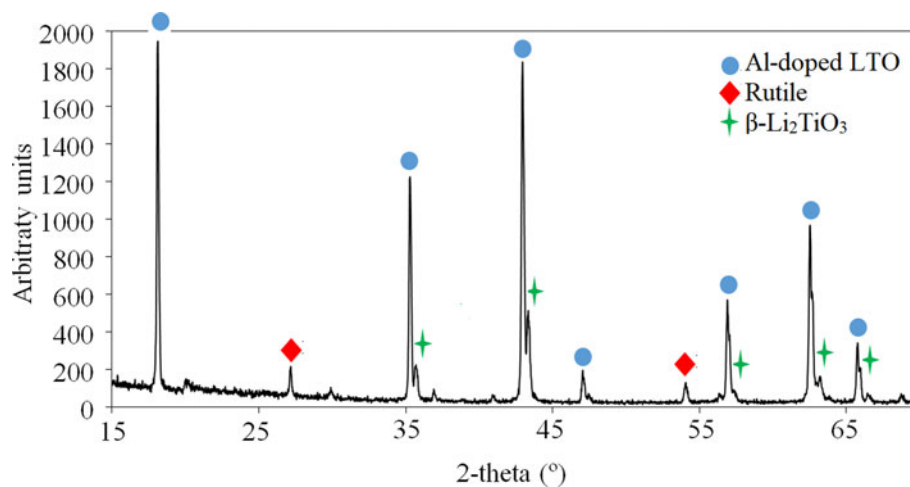


Figure 16. PXRD pattern of $\text{Li}_4\text{Ti}_{4.95}\text{Al}_{0.05}\text{O}_{12}$ at 850 °C after 4 h showing the presence of $\beta\text{-Li}_2\text{TiO}_3$.

with the potential $\text{H}_2\text{Ti}_2\text{O}_5 \cdot \text{H}_2\text{O}$ phase (as described for $\text{Li}_4\text{Ti}_5\text{O}_{12}$) also seen in the doped material [Figure 15(b)]; however, the titanium acid is only visible between 100 and 250 °C. Similar behaviour was seen for the other doped materials, as seen from Figures 5–8.

The phases of anatase and $\text{Li}_4\text{Ti}_{4.95}\text{Ni}_{0.05}\text{O}_{12}$ are seen between 450 and 500 °C [Figure 15(c)], with rutile appearing around 550–650 °C. This corresponds to the TGA results, which show the stable LTO products forming at approximately 500 °C (Figure 2). Anatase disappears upon keeping the material at the isothermal temperature [Figure 15(e)]; however, another phase appears with a relatively strong peak close to $43^\circ 2\theta$. This peak was speculated to be the monoclinic $\beta\text{-Li}_2\text{TiO}_3$ structure (Figure 16), which is not uncommon in the synthesis of $\text{Li}_4\text{Ti}_5\text{O}_{12}$ (Laumann, 2010; Bhatti *et al.*, 2016; Li *et al.*, 2017). This was seen for all doped material; however, only appeared upon cooling for the cobalt-, nickel-, and manganese-doped lithium titanium oxides (Figure 17).

The $\beta\text{-Li}_2\text{TiO}_3$ was only observed for the doped material, which indicates that this particular sol–gel synthetic route for the doped titanates does not allow for pure doped material to be isolated. This phase appears only upon cooling the material and further investigation should be done to study methods of removing this particular phase, although a mixed phase $\text{Li}_4\text{Ti}_5\text{O}_{12}/\beta\text{-Li}_2\text{TiO}_3$ does not have a negative impact on the electrochemical characteristics of the anode material (Wang *et al.*, 2014; Bhatti *et al.*, 2016).

The phase transitions of the doped LTO materials ($\text{Li}_4\text{Ti}_{4.95}\text{M}_{0.05}\text{O}_{12}$) show similar behaviour to the undoped LTO with an initial slight decrease in the percentage phase composition of the doped LTO spinel phase between 550 and 750 °C (Figure 18). This is followed by an increase in the spinel phase composition between 750 and 850 °C with a further increase during the 4 h isothermal at 850 °C. The Al-doped spinel shows different behaviour at the isothermal stage, with the $\beta\text{-Li}_2\text{TiO}_3$ phase forming at this point already,

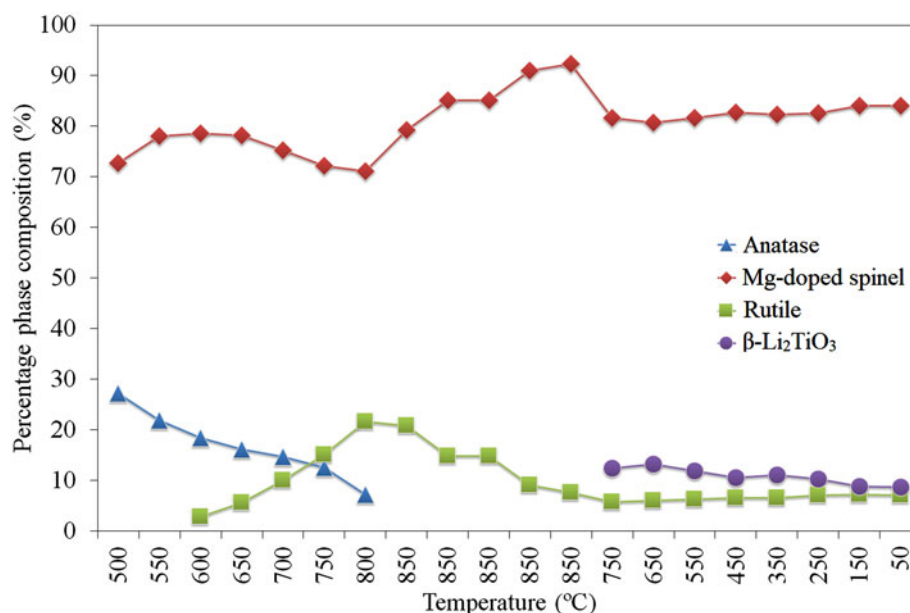


Figure 17. Percentage phase composition of the Mg-doped LTO material, rutile, $\beta\text{-Li}_2\text{TiO}_3$, and anatase from 500 to 850 °C, followed by cooling to room temperature.

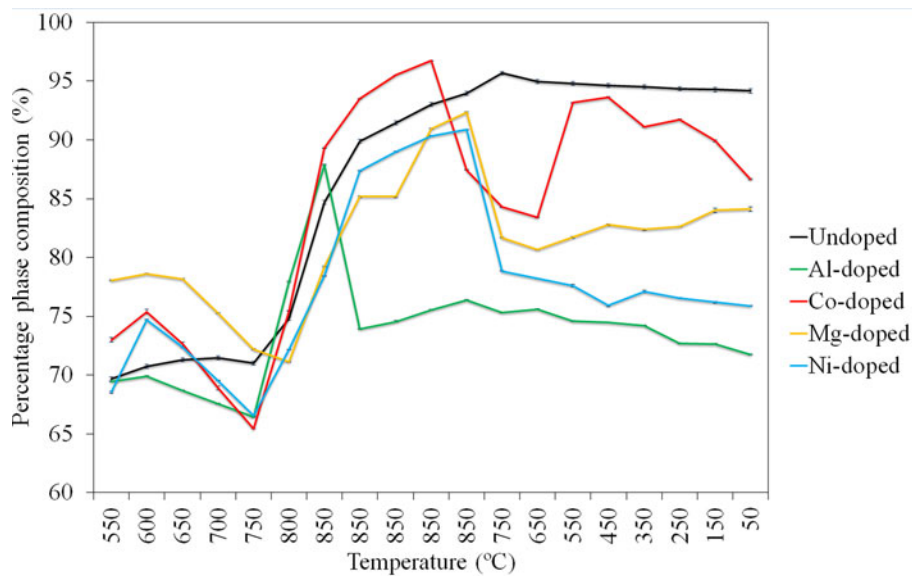


Figure 18. Percentage phase composition of the doped and undoped spinel LTO phase from 550 to 50 °C, showing error bars.

TABLE II. Summary of JMAK constants and predicted kinetics.

Sample	$\text{Li}_4\text{Ti}_5\text{O}_{12}$	$\text{Li}_4\text{Ti}_{4.95}\text{Al}_{0.05}\text{O}_{12}$	$\text{Li}_4\text{Ti}_{4.95}\text{Ni}_{0.05}\text{O}_{12}$	$\text{Li}_4\text{Ti}_{4.9}\text{Mg}_{0.05}\text{O}_{12}$	$\text{Li}_4\text{Ti}_{4.95}\text{Co}_{0.05}\text{O}_{12}$
JMAK constant					
Avrami constant (A)	0.2455	-0.4762	0.2744	0.3960	0.3054
Time constant (C) (h)	0.0372	0.0066	0.0898	0.1173	0.0363
Predicted time to form an almost pure spinel phase (h)	18.7	(102.7) ^a	23.4	20.4	5.4

^aBased on the decrease in rutile phase.

resulting in a lower spinel phase composition compared to the other material. The change in the LTO spinel phase formation during the 850 °C isothermal period can be described by the Johnson–Mehl–Avrami–Kolmogorov (JMAK) kinetic equation, as illustrated in the equation [see Eq. (2)], where $P_{(\%)}$ is the percentage phase composition of the doped/undoped LTO phase, t is the time in hours, A is the Avrami exponent,

and C is the time-dependent constant.

$$P_{(\%)} = 1 - e^{(-t)^A} \quad (2)$$

This kinetic relationship is often used to describe crystal growth (Starink, 2001; Ahmad *et al.*, 2014) and can be

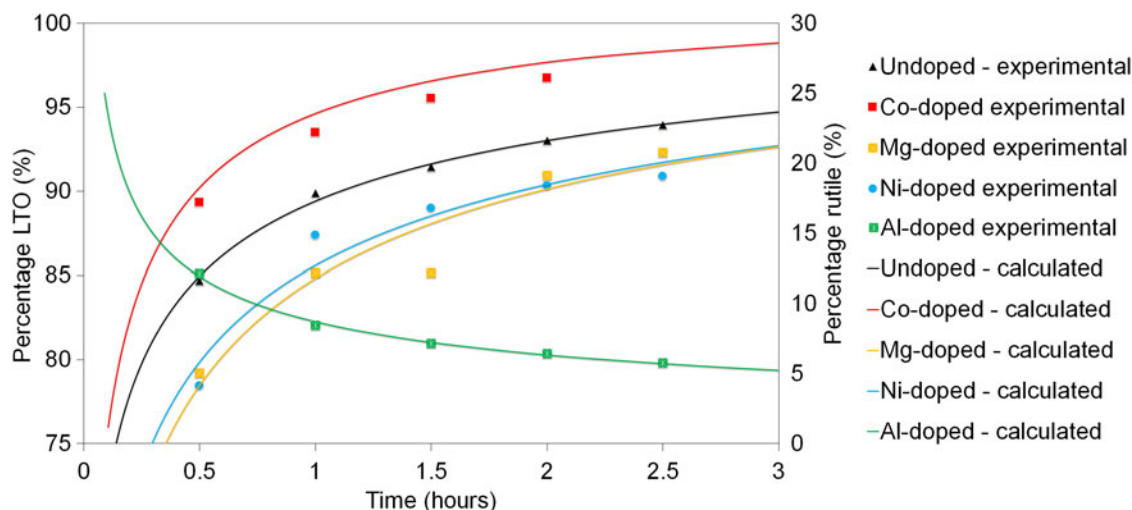


Figure 19. The calculated LTO phase formation curves with their experimental data from *in situ* analysis for undoped, Co-, Mg-, and Ni-doped material. The decreased rutile is shown for the Al-doped analogue on the secondary axis.

TABLE III. Final proposed and nominal chemical composition for doped materials.

Dopant used	Nominal formula	Final proposed chemical composition
Al-doped (Al ³⁺)	Li ₄ Ti _{4.95} Al _{0.05} O ₁₂	Li ₄ Ti _{4.95} Al _{0.05} O _{11.95}
Ni-doped (Ni ²⁺)	Li ₄ Ti _{4.95} Ni _{0.05} O ₁₂	Li ₄ Ti _{4.95} Ni _{0.05} O _{11.925}
Mg-doped (Mg ²⁺)	Li ₄ Ti _{4.95} Mg _{0.05} O ₁₂	Li ₄ Ti _{4.95} Mg _{0.05} O _{11.925}
Co-doped (Co ³⁺)	Li ₄ Ti _{4.95} Co _{0.05} O ₁₂	Li ₄ Ti _{4.95} Co _{0.05} O _{11.95}

transformed into its linear form [see Eq. (3)] to solve the constants A and C from the slope and y-axis intercept, respectively.

$$\ln\left(\ln\left(\frac{1}{1-P_{(\%)}}\right)\right) = A \ln t - A \ln C \quad (3)$$

The calculated Avrami exponent and time-dependent constant values for the synthesized materials are tabulated in Table II, with the sigmoidal curve illustrated in Figure 19 which depict both the calculated and experimental phase formation as a function of time. The predicted kinetic behaviour of the undoped material, as well as the nickel-, manganese-, and cobalt-doped analogues, show that the material should form a highly pure spinel phase if allowed to react up to 24 h at a constant temperature of 850 °C. This suggests that after drying the precursor material in the synthetic route of the lithium titanates to 300 °C, the material should be slowly heated to 850 °C and remain there for a minimum of 24 h to effectively remove any rutile present. Rutile can negatively impact the battery performance due to its influence on lithium-ion diffusion (Syahrial *et al.*, 2016) and should, therefore, ideally be removed completely. The results are based on an *in situ* study only and laboratory experiments or large-scale processes could yield different results; however, based on the literature, extensive heating does reduce the rutile content or

eliminates it completely (Hao *et al.*, 2005; Mahmoud *et al.*, 2015; Sun *et al.*, 2015). A typical literature reports on calcining such samples at 800 °C and higher for 12–24 h (Hao *et al.*, 2005; Sun *et al.*, 2015). Some have found that an hour at 900 °C was also sufficient to eliminate the rutile phase in the LTO material (Mahmoud *et al.*, 2015). The aluminium-doped material indicated that a fair amount of the rutile phase was still present at the high temperatures and would take a significantly long time to obtain the pure product. The β -Li₂TiO₃ also appears at the isothermal temperature, which results in much lower pure LTO, therefore for the Al-doped material, the decrease in rutile is shown in Figure 19. This was different from what was reported in the literature (Lin *et al.*, 2013) and the difference could be ascribed to the analytical method used for the particular sample. Li₄Ti_{4.95}Al_{0.05}O₁₂ was synthesized using a different sol-gel methodology (Hao *et al.*, 2005) than that reported in the literature, where the literature reported doped material showed no rutile when calcining at 800 °C for 12 h (Lin *et al.*, 2013). The presence of β -Li₂TiO₃, according to the literature, can effectively be removed by calcining at 900 °C for at least 2 h (Laumann *et al.*, 2011), which explains why it was detected as a minor impurity in the doped material.

The proposed final chemical composition of the doped spinel material can be found in Table III, which illustrates that the final proposed chemical composition of the material differs slightly from the nominal formula (as reported throughout the paper), due to the oxygen vacancy created by the substitution of dopants with lower valences into Ti⁴⁺ sites, as required by the charge neutrality condition (Hao *et al.*, 2008; Wang *et al.*, 2011). The Mg²⁺ and Ni²⁺ will result in a larger oxygen vacancy, compared to Al³⁺ and Co³⁺, as evident from the proposed formula (Table III). The crystallite sizes (LVol-IB) as determined by the full pattern Rietveld refinement for both the undoped and doped LTOs are graphically illustrated in Figure 20, from 550 °C where the spinel phase was initially identified up to 850 °C, and subsequent

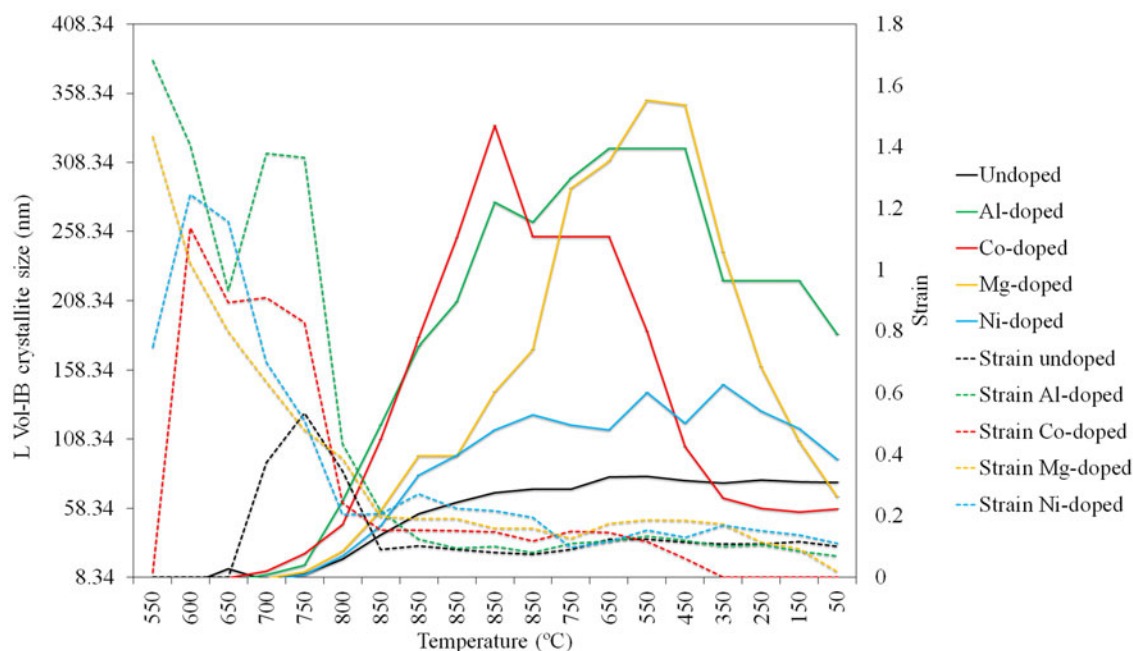


Figure 20. Crystallite size (LVol-IB) (nm) of the *in situ* X-ray diffraction results for the undoped and doped lithium titanium oxide material.

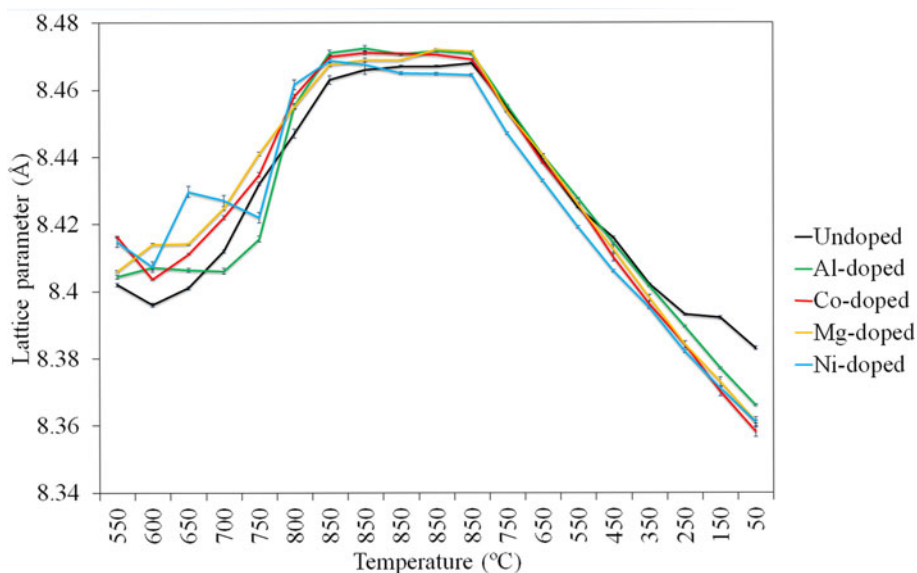


Figure 21. Unit-cell lattice parameter (Å) of the *in situ* X-ray diffraction results for the undoped and doped lithium titanium oxide material, showing error bars.

cooling to 50 °C. For the undoped LTO, the change in the crystallite size with temperature showed an approximate $0.120 \text{ nm } ^\circ\text{C}^{-1}$ increase when heating from 550 to 850 °C. A further increase to 72.21 nm was observed when leaving the sample at 850 °C for 4 h. Similar behaviour was seen for the doped LTO analogues; however, by comparison, the aluminium, cobalt, and magnesium-doped spinel material showed significantly higher crystallite sizes over the temperature range. As the material is kept at the isothermal temperature (850 °C), the crystallite size is seen to increase, which suggests that an increase in reaction time results in an increase crystallite size and has been observed in lithium titanates before (Nugroho *et al.*, 2014). Cooling the undoped material shows little to no changes in crystallite size; however, the doped material shows a decrease, which can be due to the combined effect of rapid cooling of the material, sample shrinkage and the lattice constraints that is induced upon doping (Figure 17) (Hatfield *et al.*, 1971; Karhunen *et al.*, 2016). During the least-squares refinement process in Topas, the L-strain parameter was allowed to refine, which increased as the LTO formation progresses from 550 to 850 °C. Once the material reaches the isothermal temperature range, the strain parameter refined to a minimal value and was relatively constant until the material was cooled to 50 °C. Similar trends in the unit-cell lattice parameters for $\text{Li}_4\text{Ti}_5\text{O}_{12}$ - and $\text{Li}_4\text{Ti}_{4.95}\text{M}_{0.05}\text{O}_{12}$ -doped materials were observed with a slight increase (0.63–0.75%) over the temperature range from 550 to 850 °C. A decrease between 0.085 and 0.11 Å in unit-cell lattice parameters were observed when the samples were cooled to 50 °C (Figure 21). The change in unit-cell parameter directly correlates to the change in temperature (Huynh *et al.*, 2019), due to the unit-cell expansion or contraction upon heating or cooling. At the constant temperature of 850 °C, a relatively constant unit-cell lattice parameter was observed. It is expected that the unit-cell parameter will decrease upon doping with the Co^{3+} and Al^{3+} as it has a smaller ionic radii compared to that of Ti^{4+} (Park *et al.*, 2014; Guo *et al.*, 2016); which correlates with the results found (Figure 21). The decreasing unit-cell parameter upon doping with larger ions Mg^{2+} and Ni^{2+} shows anomalous

behaviour as it is expected to increase (Li *et al.*, 2015; Abureden *et al.*, 2016), which can be the result of the difference valences of the titanium ions and the doping cations. The strain parameter determined in this study is relative. It shows that the material upon heating and when undergoing phase transitions, simultaneously undergoes crystallite size growth and stress/strain properties within its crystal domain.

IV. CONCLUSION

The *in situ* PXRD temperature studies of forming the spinel LTO and its doped analogues made from its precursor gel-based materials showed that it was predominantly amorphous from room temperature up to 450 °C, with a small amount of an intermediate crystalline phase that was identified to be a type of titanium acid ($\text{H}_2\text{Ti}_2\text{O}_5 \cdot \text{H}_2\text{O}$). Upon further heating, the intermediate phase disappeared and the formation of anatase and the spinel LTO was observed. Rutile appeared to form around 550 to 650 °C, with sharp, distinct peaks of the spinel phase only seen at 850 °C coupled with the disappearance of the anatase phase. The broader diffraction peaks of the spinel phase were observed around 650 °C and would typically correspond to a material with a small crystallite size. This was confirmed by observing a significant decrease in the material's surface areas that were synthesized at 650 and 850 °C, as well as SEM images of the respective materials, where a conglomeration of the crystals was observed for the material made at the higher temperature.

When maintaining the material isothermally at 850 °C for a number of hours, a decrease of the rutile phase was observed that could be described by a JMAK-type kinetic model. A pure LTO phase could not be isolated, as the rutile co-crystallized with the spinel material, although in minimal amounts after cooling to room temperature. The doped material had an additional titanate phase ($\beta\text{-Li}_2\text{TiO}_3$) co-crystallizing, which became more pronounced upon cooling the material, which is not uncommon in the synthesis of $\text{Li}_4\text{Ti}_5\text{O}_{12}$. Rietveld refinement of the diffraction patterns showed that the unit-cell parameters of the spinel typically increased upon heating to 850 °C, followed by a decrease upon cooling that was in

agreement of published unit-cell parameters of the material at room temperature.

SUPPLEMENTARY MATERIAL

The supplementary material for this article can be found at <https://doi.org/10.1017/S0885715620000494>.

ACKNOWLEDGEMENTS

The authors express their gratitude towards the National Research Foundation and Nelson Mandela University for their financial support.

Abureden, S., Hassan, F. M., Lui, G., Ahn, W., Sy, S., Yu, A., and Chen, Z. (2016). "Multigrain electrospun nickel doped lithium titanate nanofibers with high power lithium ion storage," *J. Mater. Chem. A* **4**, 12638–12647.

Ahmad, S., Kanaujia, P., Niu, W., Baumberg, J., and Vijaya Prakash, G. (2014). "In-situ intercalation dynamics in inorganic-organic layered perovskite thin films," *ACS Appl. Mater. Interfaces* **6**, 10238–10247.

Arruda, L. B., Santos, C. M., Orlandi, M. O., Schreiner, W. H., and Lisboa-Filho, P. N. (2015). "Formation and evolution of TiO₂ nanotubes in alkaline synthesis," *Ceram. Int.* **41**, 2884–2891.

Bhatti, H. S., Anjum, D. H., Ullah, S., Ahmed, B., Habib, A., Karim, A., and Hasanain, S. K. (2016). "Electrochemical characteristics and Li⁺ ion intercalation kinetics of dual-phase Li₄Ti₅O₁₂/Li₂TiO₃ composite in the voltage range 0–3 V," *J. Phys. Chem. C* **120**, 9553–9561.

Bruker, A. (2016). *Topas Manual, Version 6.0 (Computer Software)* (Bruker Software, West Germany).

Coelho, J., Pokle, A., Park, S. H., McEvoy, N., Berner, N. C., Duesberg, G. S., and Nicolosi, V. (2017). "Lithium titanate/carbon nanotubes composites processed by ultrasound irradiation as anodes for lithium ion batteries," *Sci. Rep.* **7**, 7614.

Deschamps, A., Raveau, B., and Sekkal, Z. (1971). "Mise en évidence et étude cristallographique d'une nouvelle solution solide de type spinelle Li_{1+x}Ti_{2-x}O₄ 0 ≤ x ≤ 0, 333," *Mater. Res. Bull.* **6**, 699–704.

Dorrian, J. F., and Newnham, R. E. (1969). "Refinement of the structure of Li₂TiO₃," *Mater. Res. Bull.* **4**, 179–183.

Downs, R. T., and Hall-Wallace, M. (2003). "The American mineralogist crystal structure database," *Am. Mineral.* **88**, 247–250.

Etacheri, V., Kuo, Y., Van der Ven, A., and Bartlett, B. M. (2013). "Mesoporous TiO₂-B microflowers composed of (1 1 0) facet-exposed nanosheets for fast reversible lithium-ion storage," *J. Mater. Chem. A* **1**, 12028–12032.

Ganapathy, S., and Wagemaker, M. (2012). "Nanosize storage properties in spinel Li₄Ti₅O₁₂ explained by anisotropic surface lithium insertion," *ACS Nano* **6**, 8702–8712.

Grazulis, S., Chateigner, D., Downs, R. T., Yokochi, A. F. T., Quiros, M., Lutterotti, L., Manakova, E., Butkus, J., Moeck, P., and Le Bail, A. (2009). "Crystallography Open Database – an open-access collection of crystal structures," *J. Appl. Cryst.* **42**, 726–729.

Grazulis, S., Daškevič, A., Merkys, A., Chateigner, D., Lutterotti, L., Quirós, M., Serebryanaya, N. R., Moeck, P., Downs, R. T., and Le Bail, A. (2012). "Crystallography Open Database (COD): an open-access collection of crystal structures and platform for world-wide collaboration," *Nucleic Acids Res.* **40**, D420–D427.

Grazulis, S., Merkys, A., Vaitkus, A., and Okulič-Kazarinas, M. (2015). "Computing stoichiometric molecular composition from crystal structures," *J. Appl. Cryst.* **48**, 85–91.

Guo, Q., Wang, Q., Chen, G., Xu, H., Wu, J., and Li, B. (2016). "Molten salt synthesis of transition metal oxides doped Li₄Ti₅O₁₂ as anode material of Li-Ion battery," *ECS Trans.* **72**, 11–23.

Han, S. W., Ryu, J. H., Jeong, J., and Yoon, D. H. (2013). "Solid-state synthesis of Li₄Ti₅O₁₂ for high power lithium ion battery applications," *J. Alloys Compd.* **570**, 144–149.

Hao, Y., Lai, Q., Xu, Z., Liu, X., and Ji, X. (2005). "Synthesis by TEA sol-gel method and electrochemical properties of Li₄Ti₅O₁₂ anode material for lithium-ion battery," *Solid State Ion.* **176**, 1201–1206.

Hao, G., Li, N., Li, D., Dai, C., and Wang, D. (2008). "Study on the effect of Li doping in spinel Li_{4+x}Ti_{5-x}O₁₂ (0 ≤ x ≤ 0.2) materials for lithium-ion batteries," *Electrochem. Commun.* **10**, 1031–1034.

Haro-González, P., Pedroni, M., Piccinelli, F., Martín, L. L., Polizzi, S., Giarola, M., Mariotto, G., Speghini, A., Bettinelli, M., and Martín, I. R. (2011). "Synthesis, characterization and optical spectroscopy of Eu³⁺ doped titanate nanotubes," *J. Lumin.* **131**, 2473–2477.

Hatfield, J. D., Eades, J. L., and McClellan G. H. (1971). *Investigation of the Reactivities of Limestone to Remove Sulfur Dioxide from Fuel Gas* (Tennessee Valley Authority, Division of Chemical Development, Fundamental Research Branch, Muscle Shoals, Alabama).

Huynh, L. T. N., Ha, C. T. D., Nguyen, V. D., Nguyen, D. Q., Le, M. L. P., and Man Tran, V. (2019). "Structure and electrochemical properties of Li₄Ti₅O₁₂ prepared via low-temperature precipitation," *J. Chem.* **2019**, 7.

ICDD (2002). PDF-2 2004 (Database), edited by Dr. Soorya Kabekkodu, International Centre for Diffraction Data, Newtown Square, PA, USA.

Karhunen, T., Välikangas, J., Torvela, T., Lähde, A., and Lassi, U. (2016). "Effect of doping and crystallite size on the electrochemical performance of Li₄Ti₅O₁₂," *J. Alloys Compd.* **659**, 132–137.

Khatun, N., Anita, Rajput, P., Bhattacharya, D., Jha, S. N., Biring, S., and Sen, S. (2017). "Anatase to rutile phase transition promoted by vanadium substitution in TiO₂: a structural, vibrational and optoelectronic study," *Ceram. Int.* **43**, 14128–14134.

Koichi Momma, F. I. (2011). "VESTA 3 for three-dimensional visualization of crystal, volumetric and morphology data," *J. Appl. Crystallogr.* **44**, 5.

Kuo, Y. C., Peng, H. T., Xiao, Y., and Lin, J. Y. (2016). "Effect of starting materials on electrochemical performance of sol-gel-synthesized Li₄Ti₅O₁₂ anode materials for lithium-ion batteries," *J. Solid State Electr.* **20**, 1625–1631.

Laumann, A. (2010). *Novel Routes to Li₄Ti₅O₁₂ Spinel: Characterization and Phase Relations* (Ludwig Maximilian University of Munich, Munich).

Laumann, A., Boysen, H., Bremholm, M., Fehr, K. T., Hoelzel, M., and Holzapfel, M. (2011). "Lithium migration at high temperatures in Li₄Ti₅O₁₂ studied by neutron diffraction," *Chem. Mater.* **23**, 2753–2759.

Li, N., Liang, J., Wei, D., Zhu, Y., and Qian, Y. (2014). "Solvothermal synthesis of micro-/nanoscale Cu/Li₄Ti₅O₁₂ composites for high rate Li-ion batteries," *Electrochim. Acta* **123**, 346–352.

Li, F., Zeng, M., Li, J., and Xu, H. (2015). "Preparation and electrochemical performance of Mg-doped Li₄Ti₅O₁₂ nanoparticles as anode materials for lithium-ion batteries," *Int. J. Electrochem. Sci.* **10**, 10445–10453.

Li, S., Guo, J., Ma, Q., Yang, Y., Dong, X., Yang, M., Yu, W., Jinxian, W., and Liu, G. (2017). "Electrospun Li₄Ti₅O₁₂/Li₂TiO₃ composite nanofibers for enhanced high-rate lithium ion batteries," *J. Solid State Electrochem.* **21**, 2779–2790.

Liang, Q., Cao, N., Song, Z., Gao, X., Hou, L., Guo, T., and Qin, X. (2017). "Co-doped Li₄Ti₅O₁₂ nanosheets with enhanced rate performance for lithium-ion batteries," *Electrochim. Acta* **251**, 407–414.

Lin, J. Y., Hsu, C. C., Ho, H. P., and Wu, S. H. (2013). "Sol-gel synthesis of aluminum doped lithium titanate anode material for lithium ion batteries," *Electrochim. Acta* **87**, 126–132.

Mahmoud, A., Amarilla, J. M., and Saadoune, I. (2015). "Effect of thermal treatment used in the sol-gel synthesis of Li₄Ti₅O₁₂ spinel on its electrochemical properties as anode for lithium ion batteries," *Electrochim. Acta* **163**, 213–222.

Meagher, E. P., and Lager, G. A. (1979). "Polyhedral thermal expansion in the TiO₂ polymorphs; refinement of the crystal structures of rutile and brookite at high temperature," *Can. Mineral.* **17**, 77–85.

Merkys, A., Vaitkus, A., Butkus, J., Okulič-Kazarinas, M., Kairys, V., and Grazulis, S. (2016). "COD::CIF::Parser: an error-correcting CIF parser for the Perl language," *J. Appl. Cryst.* **49**, 292–301.

Ming, H., Ming, J., Li, X., Zhou, Q., Wang, H., Jin, L., Fu, Y., Adkins, J., and Zheng, J. (2014). "Hierarchical Li₄Ti₅O₁₂ particles co-modified with C&N towards enhanced performance in lithium-ion battery applications," *Electrochim. Acta* **116**, 224–229.

Mosa, J., Vélez, J. F., Reinoso, J. J., Aparicio, M., Yamaguchi, A., Tadanaga, K., and Tatsumisago, M. (2013). "Li₄Ti₅O₁₂ thin-film electrodes by sol-gel for lithium-ion microbatteries," *J. Power Sources* **244**, 482–487.

Ncube, N. M., Mhlongo, W. T., McCrindle, R. I., and Zheng, H. (2018). "The electrochemical effect of Al-doping on Li₄Ti₅O₁₂ as anode material for lithium-ion batteries," *Mater. Today Proc.* **5**, 10592–10601.

- Ni, H., Song, W., and Fan, L. (2016). "Double carbon decorated lithium titanate as anode material with high rate performance for lithium-ion batteries," *Proc. Natl. Sci. Mater. Int.* **26**, 283–288.
- Nugroho, A., Chung, K. Y., and Kim, J. (2014). "A facile supercritical alcohol route for synthesizing carbon coated hierarchically mesoporous $\text{Li}_4\text{Ti}_5\text{O}_{12}$ microspheres," *J. Phys. Chem. C* **118**, 183–193.
- Park, J. S., Baek, S. H., Park, Y., and Kim, J. H. (2014). "Improving the electrochemical properties of Al, Zr Co-doped $\text{Li}_4\text{Ti}_5\text{O}_{12}$ as a lithium-ion battery anode material," *J. Korean Phys. Soc.* **64**, 1545–1549.
- Priyono, B., Syahrial, A. Z., Herman Yuwono, A., Kartini, E., Marfelly, M., and Furkon Rahmatulloh, W. M. (2015). "Synthesis of lithium titanate ($\text{Li}_4\text{Ti}_5\text{O}_{12}$) through hydrothermal process by using lithium hydroxide (LiOH) and titanium dioxide (TiO_2) xerogel," *Int. J. Technol.* **6**, 555–564.
- Rai, A. K., Gim, J., Kang, S.-W., Mathew, V., Anh, L. T., Kang, J., Song, J., Paul, B. J., and Kim, J. (2012). "Improved electrochemical performance of $\text{Li}_4\text{Ti}_5\text{O}_{12}$ with a variable amount of graphene as a conductive agent for rechargeable lithium-ion batteries by solvothermal method," *Mater. Chem. Phys.* **136**, 1044–1051.
- Shen, C. M., Zhang, X. G., Zhou, Y. K., and Li, H. I. (2003). "Preparation and characterization of nanocrystalline $\text{Li}_4\text{Ti}_5\text{O}_{12}$ by sol–gel method," *Mater. Chem. Phys.* **78**, 437–441.
- Snyders, C. D., Ferg, E. E., and Billing, D. (2016). "An investigation into the temperature phase transitions of synthesized materials with Al- and Mg-doped lithium manganese oxide spinels by *in-situ* powder X-ray diffraction," *Powder Diffr.* **32**, 23–30.
- Song, Z., Xu, H., Li, K., Wang, H., and Yan, H. (2005). "Hydrothermal synthesis and photocatalytic properties of titanium acid $\text{H}_2\text{Ti}_2\text{O}_5 \cdot \text{H}_2\text{O}$ nano-sheets," *J. Mol. Catal. A Chem.* **239**, 87–91.
- Starink, M. (2001). "On the meaning of the impingement parameter in kinetic equations of diffusion controlled reactions," *J. Mater. Sci.* **36**, 4433–4441.
- Sugimoto, T., Zhou, X., and Muramatsu, A. (2003). "Synthesis of uniform anatase TiO_2 nanoparticles by gel–sol method: 3. Formation process and size control," *J. Colloid Interface Sci.* **259**, 43–52.
- Sun, X., Radovanovic, P. V., and Cui, B. (2015). "Advances in spinel $\text{Li}_4\text{Ti}_5\text{O}_{12}$ anode materials for lithium-ion batteries," *New J. Chem.* **39**, 38–63.
- Syahrial, A. Z., Priyono, B., Yuwono, A. H., Kartini, E., Jodi, H., and Johansyah, J. (2016). "Synthesis of lithium titanate ($\text{Li}_4\text{Ti}_5\text{O}_{12}$) by addition of excess lithium carbonate (Li_2CO_3) in titanium dioxide (TiO_2) xerogel," *Int. J. Technol.* **7**, 392–400.
- Wang, Z., Chen, G., Xu, J., Lv, Z., and Yang, W. (2011). "Synthesis and electrochemical performances of $\text{Li}_4\text{Ti}_{4.95}\text{Al}_{0.05}\text{O}_{12}/\text{C}$ as anode material for lithium-ion batteries," *J. Phys. Chem. Solids* **72**, 773–778.
- Wang, W., Jiang, B., Xiong, W., Wang, Z., and Jiao, S. (2013). "A nanoparticle Mg-doped $\text{Li}_4\text{Ti}_5\text{O}_{12}$ for high rate lithium-ion batteries," *Electrochim. Acta* **114**, 198–204.
- Wang, Y., Zhou, A., Dai, X., Feng, L., Li, J., and Li, J. (2014). "Solid-state synthesis of submicron-sized $\text{Li}_4\text{Ti}_5\text{O}_{12}/\text{Li}_2\text{TiO}_3$ composites with rich grain boundaries for lithium ion batteries," *J. Power Sources* **266**, 114–120.
- Wang, C., Wang, S., He, Y.-B., Tang, L., Han, C., Yang, C., Wagemaker, M., Li, B., Yang, Q.-H., Kim, J.-K., and Kang, F. (2015). "Combining fast Li-ion battery cycling with large volumetric energy density: grain boundary induced high electronic and ionic conductivity in $\text{Li}_4\text{Ti}_5\text{O}_{12}$ spheres of densely packed nanocrystallites," *Chem. Mater.* **27**, 5647–5656.
- Wyckoff, R. W. G. (1963). *Crystal Structures* (New York, NY), 2nd ed., pp. 239–444.
- Xie, Z., Li, X., Li, W., Chen, M., and Qu, M. (2015). "Graphene oxide/lithium titanate composite with binder-free as high capacity anode material for lithium-ion batteries," *J. Power Sources* **273**, 754–760.
- Yi, T. F., Jiang, L. J., Shu, J., Yue, C. B., Zhu, R. S., and Qiao, H. B. (2010). "Recent development and application of $\text{Li}_4\text{Ti}_5\text{O}_{12}$ as anode material of lithium ion battery," *J. Phys. Chem. Solids* **71**, 1236–1242.
- Zhang, Z., Cao, L., Huang, J., Wang, D., Wu, J., and Cai, Y. (2013). "Hydrothermal synthesis of $\text{Li}_4\text{Ti}_5\text{O}_{12}$ microsphere with high capacity as anode material for lithium ion batteries," *Ceram. Int.* **39**, 2695–2698.
- Zhu, C., Liu, J., Yu, X., Zhang, Y., Zhang, Y., Jiang, X., Wang, S., Wang, Q., and Dong, P. (2019). "Enhance the electrochemical performance of $\text{Li}_4\text{Ti}_5\text{O}_{12}$ with Co doping via a facile mechanical activation strategy," *J. Mater. Sci. Mater. Electron.* **30**, 5866–5873.